2298 Vol. 59, No. 8 / 10 March 2020 / Applied Optics Research Article

applied optics

Extinction ratio and image accuracy of relayed-microgrid polarimetric imaging systems: theory and experiment

XUEQIAN SUN,[1,2,3] HE SUN,[1,2,3,*] DEJIANG WANG,[1,3] RUI WANG,[1,2] CHEN CHENG,[1,3] AND TAO ZHANG[1]

[1] Changchun Institute of Optics, Fine Mechanics and Physics, Chinese Academy of Sciences, Changchun 130033, China
[2] University of Chinese Academy of Sciences, Beijing 100049, China
[3] Key Laboratory of Airborne Optical Imaging and Measurement, Changchun Institute of Optics, Fine Mechanics and Physics, Chinese Academy of Sciences, Changchun 130033, China
*Corresponding author: sunhe_ciomp@163.com

Received 17 December 2019; revised 27 January 2020; accepted 27 January 2020; posted 27 January 2020 (Doc. ID 386216); published 2 March 2020

Herein we propose a polarimetric imaging system that uses a microgrid polarizer placed on the conjugate point of two telecentric optical paths, matching large polarizers with small sensors and thus effectively decreasing optical crosstalk and increasing imaging accuracy. We define a new parameter used to construct the high-precision polarization vector transfer model under crosstalk. Using the equivalent surface of the detector, we establish the relationship between focal shift and crosstalk ratio and obtain a multi-physical coupling mathematical model that accounts for the crosstalk ratio, extinction ratio, sensor error, target vector, and imaging accuracy of the system. The relayed-microgrid polarimetric imaging system is anticipated to be able to help identify objects of interest for remote sensing and military applications.

https://doi.org/10.1364/AO.386216

1. INTRODUCTION

Owing to improvements in nanotechnology, polarimetric imaging systems based on nanowire filters are now extensively used in biomedicine, environmental engineering, and military applications [1–8]. These types of imaging systems adopt pixel-level mosaic polarimetric modulation schemes. The microgrid polarizer is integrated into the focal plane with a pattern of linear polarizers set at 0°, 45°, 90°, and 135° [9]. The mainstream focal-divide polarimetric imaging systems are divided into two types: chipped and mounted [10–12]. The chipped polarimetric imaging system directly places the microgrid polarizer on top of the photodiode to achieve realization on a single chip, such as Sony's PL-D755MU-POL machine vision polarimetric camera [13]. The chipped imaging system yields a high extinction ratio (ER), but the production process is complex and difficult to customize. The mounted polarimetric imaging system (MPIS) places the microgrid polarizer between the on-chip lens and the external protective glass. The MPIS can be customized for different sizes of sensors (different number of pixels). However, owing to the fluctuation of the light and the small aperture of the microgrid polarizer, optical crosstalk occurs on the focal plane [14]. The crosstalk between adjacent pixels increases the uncertainty in the measured polarization states in a scene of interest.

Cruz-Cabrera *et al.* [14] have proved that the crosstalk is considerably affected by the pixel size. However, according to their theory, although a traditional polarimetric imaging system could suppress crosstalk by enlarging the pixel size, it would reduce the spatial resolution of the polarimetric image. It also has limited use in sensitive applications where high signal strength is necessary, because polarizers permanently reduce signal strength and therefore range. Thus, we propose herein the concept of the relayed-microgrid polarimetric imaging system (Re-MPIS). Utilizing the zoom ratio of the dual telecentric relay system, it integrates larger microgrid polarizers on small sensors and thus effectively reduces optical crosstalk and increases imaging accuracywhile maintaining spatial resolution. The Re-MPIS can also realize multimodal imaging by switching different filters, moving them in and out of the optical path. Compared with traditional polarimetric imaging systems, it has a greater scope for application.

Over the past year, many researchers have paid attention to simulations of crosstalk in microgrid polarizers [14–16]. However, most of the published studies focus on the behavior of the pixel performance as a function of the wire-grid count, metal density, and pixel size. Although researchers have used transmission to express the intensity of crosstalk below a certain wavelength, the transmission changes as the wavelength range

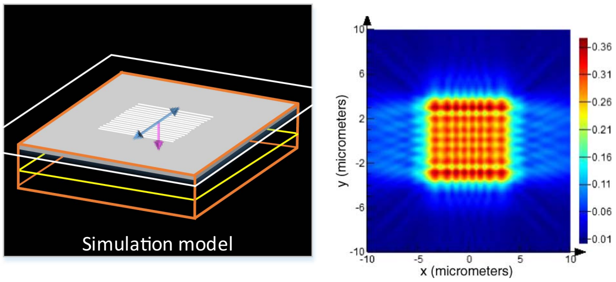

(a) (b)

Fig. 1. (a) Axonometric drawing of the simulated structure showing the glass substrate and aluminum polarizer structure, in which the double-ended arrows show the orientation of the light source polarization vector, while the downward arrow shows the direction of propagation. The area enclosed by the white line represents the light resource, the area enclosed by the orange line represents the simulation space, and the area enclosed by the yellow line represents the monitor. (b) Electric field distribution on a monitor.

changes with random behavior. We are interested in the definition of a proportional parameter that could directly reflect the relationship between the degree of crosstalk and the target light. Thus, in Sections 2.A and 2.B we quantify the near-field diffraction effects of the polarizer apertures to introduce a new parameter, the crosstalk ratio, and we then establish a mathematical transfer matrix model in the presence of crosstalk.

In recent research on the imaging error of the polarimetric imaging system, Sun *et al.* [17] studied the effect of the sensor's signal-to-noise ratio (SNR) and ER on the polarimetric imaging error. Additionally, Perkins and Gruev [18] developed methods to correct fixed-pattern nonuniformity errors. They all attributed crosstalk to the nonuniformity of the system and eliminated the error based on corrections. However, when the target is in a cold, deep-space environment, or the contrast between the target and the background is not significant, crosstalk will considerably affect the imaging accuracy. Thus, in Section 2.D, we establish a mathematical model of the coupling action of multiple physical quantities, including the ER, crosstalk ratio, random errors, polarizations of the target, and imaging accuracy. Compared with the existing mathematical models, it has a greater scope for application and produces more accurate solutions. To verify the mathematical model and simulation results, we have built the MPIS and Re-MPIS experimental platforms to measure the ER and the polarization accuracies of the two systems.

2. SIMULATION, MODELING, AND THEORETICAL DERIVATION

A. Simulation of Crosstalk

To quantify the crosstalk between adjacent pixels of microgrid polarizers, we need to define a parameter to represent the degree of optical crosstalk, which can then be used to establish the mathematical model with high precision.

We used Lumerical finite-difference time-domain (FDTD) solutions to simulate the propagation process of light in a single polarizer [15]. Figure 1(a) depicts a single microgrid polarizer with a size of 10 μm × 10 μm. The structures were constructed with a thin aluminum layer, and the metal wires were created by "etching" transparent trenches in the aluminum layer. This resulted in structures with metal wires and opaque regions around each pixel that mimic the actual polarizers. We simulated the response of a square polarizer unit (with a side of 5 μm and wire widths equal to 100 nm). The spacings of the wires were equal to their widths (50% duty cycle). A polarized broadband light pulse was propagated from its origin 3 μm above the aluminum wire layer in the downward direction. The throughput of the pixel was measured using a two-dimensional (2D) electric field monitor 2 μm below the aluminum with a size of 20 μm × 20 μm.

It can be observed in Fig. 1(b) that the diffraction effects of the microgrid polarizers are very strong. Moreover, the intensity of crosstalk is related to the orientation of the grid. This is attributed to the polarizer given that the strictly defined boundary conditions are associated with a prominent diffraction effect.

Next, we simulate two polarizers with different orientations to observe optical crosstalk in a superpixel. We establish the two superpixel models consisting of polarizer pixels with a 6 μm side and 1 μm wide opaque regions that separate four individual pixels (pixel A, pixel B, pixel C, and pixel D). As shown in Fig. 2(a), the effective dimensions of individual pixel equal 5 μm × 5 μm. The wires had a width and a spacing of 100 nm and a height of 100 nm. Four 2D electric field monitors (with a size of 5 μm × 5 μm) were placed at distances of 1 μm below the aluminum wire layer, corresponding to the position of each pixel, and were used to record the transmittance of each pixel. The value was used to calculate the crosstalk ratio to estimate the amount of diffracted light.

The polarized light source with a polarization angle of 0° (for the first model) and 135° (for the second model) from its origin was placed 3 μm above the aluminum wire layer, emitting in a downward direction. In the simulation process, the monitors were moved at 0.5 μm intervals up to 10 μm in the axial direction. Transmittance values at each distance were used for the plots.

The transmittance of the microgrid polarizer was stable at around 0.67, and the adjacent pixels could also receive some photoelectrons owing to the optical crosstalk. The curves in Fig. 3 with different colors differed by an order of magnitude regarding the evoked transmittance values, while the curves of pixel A′ and pixel D′ are well coincident. It was confirmed that the strength of diffraction was largely determined by the diffraction distance. The data shows that the amount of light increases by 16.7 times when the monitor is moved from 1 to 10 μm away from the polarizer. This seriously affects the polarization information response model of the system.

According to the simulation result, we define the new parameter χ to describe the degree ofcrosstalk, which can be calculated as the ratio of the transmittance T between adjacent pixels. $T_{\text{non-etched}}$ represents the transmittance of non-etched pixels under crosstalk, such as the transmittance of pixel A, pixel A′. T_{etched} represents the transmittance of etched pixels, such as the transmittance of pixel B, pixel B′, corresponding to Figs. 2(a) and 2(b). The equation for parameter χ is

$$\chi = T_{\text{non-etched}} / T_{\text{etched}}. \quad \textbf{(1)}$$

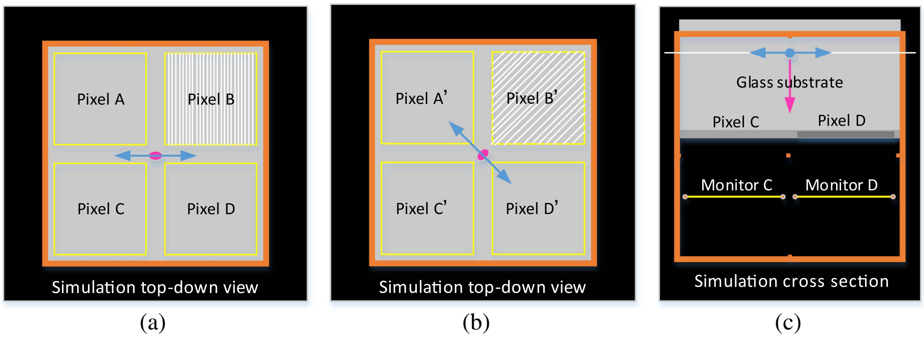

(a) (b) (c)

Fig. 2. (a) First model, etching of the wire grid at 90° at the upper right corner. The other three pixels are left unetched. (b) Second model, etching of the wire grid at 45° at the upper right corner. The other three pixels are left unetched. (C) Cross-section view of the simulation.

The definitions of parameter χ at different orientations can be seen in Fig. 4.

There are five kinds of crosstalk between pixels as shown in Figs. 4(a) and 4(b). For example, in Fig. 4(a), the green arrow points from the etched pixel to the pixel vertical to the grid orientation; the crosstalk parameter in that case is defined as χ_a, where $\chi_a = T_{\text{pixel A}}/T_{\text{pixel B}}$. Accordingly, the crosstalk from the etched pixel to the pixel parallel to the grid orientation is expressed by χ_b (red arrow), where $\chi_b = T_{\text{pixel D}}/T_{\text{pixel B}}$. The crosstalk from the etched pixels to the oblique pixels is expressed by χ_c (yellow arrow), where $\chi_c = T_{\text{pixel C}}/T_{\text{pixel B}}$. In Fig. 4(b), the crosstalk from the etched pixel to the vertical and parallel pixels is expressed by χ_d (blue arrow), where $\chi_d = T_{\text{pixel A}'}/T_{\text{pixel B}'}$, and so on. The crosstalk from the etched pixels to the oblique pixels is expressed by χ_e (purple arrow), where $\chi_e = T_{\text{pixel C}'}/T_{\text{pixel B}'}$. As shown in Fig. 4(c), i represents the row of the polarizer array, and j represents the column of the array. Each pixel of the polarizer is interfered by the surrounding pixels and also produces a crosstalk effect on the surrounding pixels. The aliasing effect of these crosstalks is the cause of the low crosstalk ratio of the polarizer and poor accuracy of the imaging system.

B. Polarization Vector Transfer Model

Based on the definition listed above, we can obtain the crosstalk matrix M_c given by

$$M_c = \begin{bmatrix} 1-2\chi_a-4\chi_c-2\chi_b & 2\chi_d & 4\chi_c & 2\chi_d \\ 2\chi_b & 1-4\chi_e-4\chi_d & 2\chi_b & 4\chi_e \\ 4\chi_c & 2\chi_d & 1-2\chi_a-4\chi_c-2\chi_b & 2\chi_d \\ 2\chi_a & 4\chi_e & 2\chi_a & 1-4\chi_d-4\chi_e \end{bmatrix}. \tag{2}$$

Establishment of the polarization vector transfer model, including the crosstalk matrix, leads to

$$I_{\text{out}} = M_c M_f S_{\text{in}}. \tag{3}$$

We use the Stokes vector notation S_{in} to describe the target signal [19]. M_f represents the Muller matrix of the polarizer [2]. I_{out} represents the intensity matrix of a superpixel on the sensor, consisting of the photoelectronic numbers $PN_{i,j}{}^{\text{out}(\theta)}$ received by the sensor pixel of the ith row and the jth column. θ represents the etching angle of the polarizer. Compared with the traditional Muller matrix transfer model, this model changes the inherent proportion relationship in the transfer matrix and has a higher accuracy. In addition, the relationship between the PN received by the different pixels in one superpixel and the input target light polarization state (i.e., the degree and angle of linear polarization, DOLP and AOLP) is given by

$$\text{AOLP}^{\text{in}}{}_{i,j} = 0.5 \times \frac{180}{\pi} \times \arctan \frac{\left[(\text{PN}_{i,j}{}^{\text{out}}{}_{(0)} - \text{PN}_{i+1,j+1}{}^{\text{out}}{}_{(90)}) \times (1+4\chi_c) \times (1-4\chi_d-4\chi_e)\right]}{\left[(\text{PN}_{i+1,j}{}^{\text{out}}{}_{(45)} - \text{PN}_{i,j+1}{}^{\text{out}}{}_{(135)}) \times (1+4\chi_e) \times (1\text{-}2\chi_a-4\chi_c-2\chi_b)\right]}, \tag{4}$$

$$\text{DOLP}^{\text{in}}_{i,j} = \frac{2}{\text{x}_{i,j}} \times \frac{\sqrt{\left[\frac{(\text{PN}_{i,j}{}^{\text{out}}{}_{(0)}-\text{PN}_{i+1,j+1}{}^{\text{out}}{}_{(90)})\times(1+4\chi_c)}{(1-2\chi_a-2\chi_b-4\chi_c)}\right]^2 + \left[\frac{(\text{PN}_{i+1,j}{}^{\text{out}}{}_{(45)}-\text{PN}_{i,j+1}{}^{\text{out}}{}_{(135)})\times(1+4\chi_e)}{(1-4\chi_d-4\chi_e)}\right]^2}}{\left(\text{PN}_{i,j}{}^{\text{out}}{}_{(0)} + \text{PN}_{i+1,j+1}{}^{\text{out}}{}_{(90)} + \text{PN}_{(i+1,j)}{}^{\text{out}}{}_{(45)} + \text{PN}_{i,j+1}{}^{\text{out}}{}_{(135)}\right)}, \tag{5}$$

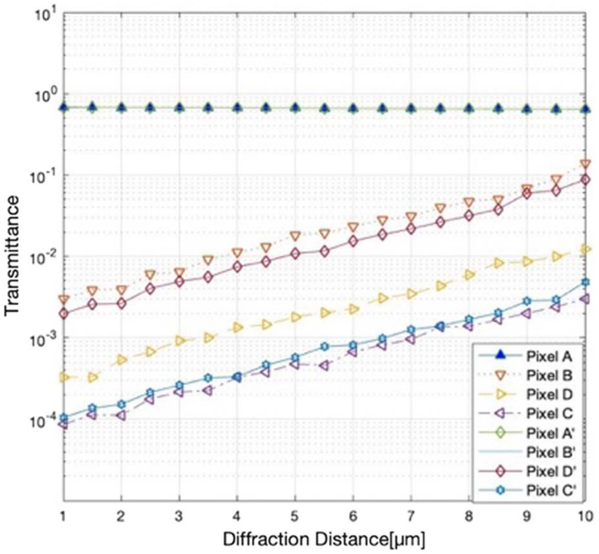

Fig. 3. Transmittance curves.

where $x_{i,j}$ is the diattenuation of one nanowire filter in the superpixel. It can be observed that the crosstalk affects the resolved polarization states of the target.

C. Optical Wave Field Propagation of the Re-MPIS

Based on the work of Cruz-Cabrera *et al.* [14], increasing the size of polarizer can effectively reduce the influence of optical crosstalk on the accuracy of imaging. Thus, we propose Re-MPIS. The optical structure is shown in Fig. 5. First, the polarizer aperture size was enlarged to reduce the optical crosstalk, and the zoom ratio of the relay system was then utilized to reduce the point size that corresponded to the sensor pixel size.

In this case, U_0 represents the wave function when the beam enters the optical system, U_1 represents the wave function at the actual location of the polarizer, U_2 represents the wave function at the primary image plane, U_3 represents the wave function when the beam enters the relay system, U_4 represents the wave function at the aperture diaphragm, U_5 represents the wave function when the beam exits the relay system, U_6 represents the wave function at the second image plane, and d represents the focal shift in the relay system (which is approximately equal to ±2 μm according to the precision of the machinery components).

To explore the influence of focal shifts on imaging, we modeled the optical wave field propagation of Re-MPIS. Given that the imaging target is at a long distance away from the imaging system, it can be considered that the beam is emitted in the form of parallel rays, given different incident angles. The parallel light emitted from the long-distance target enters the system. Different object points on the target correspond to parallel beams of different fields of view, which are imaged on the metal wire grating by the pre-system;

$$U_2(x_0, y_0) = U_1(x_0, y_0)t(x_0, y_0), \tag{6}$$

where x_0, y_0 are the coordinates in U_2 and $t(x_0, y_0)$ is complex amplitude transmittance function of microgrid polarizer. According to the effect medium theory (EMT), [20,21] the structures of the microgrid polarizer are equivalent to a matrix aperture with a certain transmittance

$$t = \mathrm{rect}\left(\frac{x_0}{a}\right)\mathrm{rect}\left(\frac{y_0}{a}\right), \tag{7}$$

where a is the length of the matrix aperture. Due to the focal shift d existing in the optical path, the process of diffraction can be regarded as a Fresnel approximation:

$$\begin{aligned} U_2(x_0, y_0) &= \frac{1}{j\lambda d}\exp(jkd)\exp\left[j\frac{k}{2f}({x_0}^2 + {y_0}^2)\right] \\ &\quad \times \sin c\left(\frac{a x_0}{\lambda d}\right)\sin c\left(\frac{a y_0}{\lambda d}\right), \\ \Delta x &= \Delta y = 2\frac{\lambda d}{a}, \end{aligned} \tag{8}$$

where λ is the wavelength of incident light, d is diffraction distance, k is wave number, $k = 2\pi/\lambda$, and Δx and Δy represent the size of the central bright spot; as a becomes smaller, the diffraction becomes more significant.

From U_2 to U_4, the wave function performs a Fourier transform:

$$U_4 = \Im\{U_2\} \propto \iint U_2 \exp\left[\frac{-ik}{F}(x_0\xi + y_0\eta)\right]\mathrm{d}x_0\mathrm{d}y_0, \tag{9}$$

where ξ, η are the coordinates in U_4. From $U4$ to $U6$, the wave function performs another Fourier transform:

$$\begin{aligned} U_6 &= \Im\{U_4\} \\ &\propto \iint U_4 \exp\left[\frac{-ik}{f}(x'\xi + y'\eta)\right]\mathrm{d}\xi\mathrm{d}\eta \\ &\propto \iiiint U_2 \exp\left[\frac{-ik}{f}[(x_0 + x')\xi + (y_0 + y')\eta)]\right]\mathrm{d}x_0\mathrm{d}y_0\mathrm{d}\xi\mathrm{d}\eta \\ &\propto U_2(-x', -y'), \end{aligned} \tag{10}$$

where x', y' are the coordinates in U_6. Fraunhofer diffraction occurred from U_2 to U_4 that caused frequency division. Another Fraunhofer diffraction occurred from U_4 to U_6 that caused light combination. Two consecutive Fourier transforms restore the function, and the image is inverted. Thus, U_2 can be regarded as the equivalent focal plane, whereby the focal shift is similar to the diffraction distance in MPIS.

By enlarging the pixel size of the microgrid polarizer, the crosstalk could be suppressed effectively, which could be verified by the simulation that is presented next. The modeling process is similar to that in Section 2.A. We simulated superpixels that consisted of polarizer pixels with 12 μm pitches and 2 μm wide opaque regions, which were etched only at the upper right corner. The microstructures and sources were the same as those used in Section 2.A. The monitor size is 10 μm × 10 μm. We use the simulation results of Sections 2.A and 2.C to calculate crosstalk as shown in Fig. 6 .

Comparison of the two kinds curves shows that the polarizer with the larger size yielded a lower sensitivity to crosstalk. For the

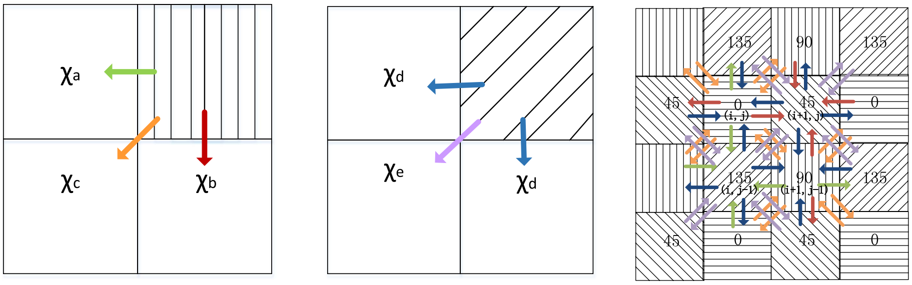

(a) (b) (c)

Fig. 4. (a) Graphic expression of χ_a, χ_b, and χ_c. (b) Graphic expression of χ_d and χ_e. (c) Superimposed crosstalk between pixels.

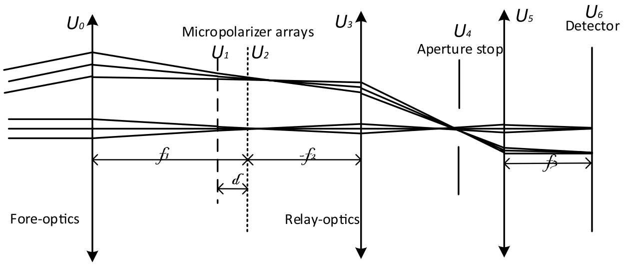

Fig. 5. Optical structure of the proposed imaging system.

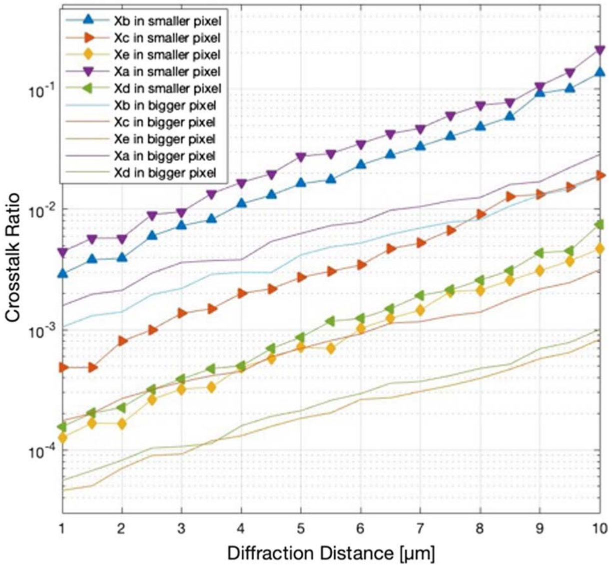

Fig. 6. Crosstalk ratio of superpixels with two sizes.

same diffraction distance, the crosstalk was only 1/3 to 1/4 of the value evoked when the polarizer size was 5 μm × 5 μm. Thus, it is effective to reduce optical crosstalk using a relay optical structure in the microgrid polarimetric imaging system.

Based on this structure, the system can realize multimodal imaging. The shutter mechanism may include any mechanism that can be used to reliably and repeatably move the microgrid polarizer in and out of the optical path to provide a polarimetric or a standard intensity image in an alternate manner. Moreover, the system may include one or more filter arrays, such as the neutral density filter or Bayer arrays. Each array may be independently switched in and out of the optical path to realize multimodal imaging. This structure has practical and theoretical significance, since some targets are more obvious in the polarization mode while other targets are more obvious in the intensity mode. The two modes complement each other and significantly improve the ability of target searching.

D. Theoretical Analysis of the Accuracy of the Imaging System

In prior sections, we established the relationship between the focal shift and crosstalk ratio. However, a complete polarization vector transfer model is still lacking the connection between the imaging accuracy of the entire system and the physical factors that affect the imaging quality, such as sensor errors, extinction ratio, crosstalk ratio, and the polarization of the target.

In the case of a scientific imaging sensor, the random error was composed of shot, dark, and read noise. The sum of the dark and read noise in scientific sensors is usually less than 0.05% of the full-well capacity [17]. In this case, we only need to consider the shot noise. Thus, the variance of the received photons was caused by the shot noise alone and followed a Poisson distribution, where $\sigma_{\mathrm{shot}} = \sqrt{\mathrm{PN}}$ [18]. Thus, $\mathrm{SNR} = \mathrm{PN}/\sigma_{\mathrm{shot}} = \sqrt{\mathrm{PN}}$ [22].

We used error propagation methods to determine the uncertainty in the AOLP and DOLP. If we consider the error propagation of the AOLP as an example, we have

$$\begin{aligned}\mathrm{NeAolp}_{i,j} = {} & \left(\frac{\partial \mathrm{AOLP_{in}}}{\partial \mathrm{PN}_{i,j}{}^{\mathrm{out}}{}_{(0)}}\right) * \sigma^2{}_{\mathrm{PN}_{i,j}{}^{\mathrm{out}}{}_{(0)}} \\ & + \left(\frac{\partial \mathrm{AOLP_{in}}}{\partial \mathrm{PN}_{i,j+1}{}^{\mathrm{out}}{}_{(90)}}\right) * \sigma^2{}_{\mathrm{PN}_{i,j}{}^{\mathrm{out}}{}_{(90)}} \\ & + \left(\frac{\partial \mathrm{AOLP_{in}}}{\partial \mathrm{PN}_{i+1,j}{}^{\mathrm{out}}{}_{(45)}}\right) * \sigma^2{}_{\mathrm{PN}_{i,j}{}^{\mathrm{out}}{}_{(45)}} \\ & + \left(\frac{\partial \mathrm{AOLP_{in}}}{\partial \mathrm{PN}_{i+1,j+1}{}^{\mathrm{out}}{}_{(135)}}\right) * \sigma^2{}_{\mathrm{PN}_{i,j}{}^{\mathrm{out}}{}_{(135)}}. \end{aligned} \quad \textbf{(11)}$$

$\mathrm{NeAolp}_{i,j}$ is the variance of the AOLP in the time domain. Equations (4) and (5) are complex expressions. To simplify the reduction process, we propose the concept of the average crosstalk ratio $\bar{\chi}$ to simplify the PN received by sensors:

$$\bar{\chi}_{i,j} = (\chi^{0}_{i,j} + \chi^{45}_{i,j} + \chi^{90}_{i,j} + \chi^{135}_{i,j})/4, \tag{12}$$

$$\mathrm{PN}^{\mathrm{out}}{}_{(\theta)} = 0.5 * \beta * S0_{\mathrm{in}} * (\varepsilon + \eta) * \left\{1 + \frac{\varepsilon - \eta}{\varepsilon + \eta} * \mathrm{Dolp}^{\mathrm{in}} * \cos[2(\theta - \varphi)]\right\} * (1 + \bar{\chi}), \tag{13}$$

where ε is the transmittance of the pass axis, η is the transmittance of the stop axis, and φ is the polarization angle of the input target light [15]. By combining Eqs. (4), (11), and (13), we can obtain

$$\mathrm{NeAolp}_{i,j} = \frac{S0_{\mathrm{in}} \cdot (\mathrm{ER} + 1) + 2\frac{\bar{\chi}}{\eta}}{[S0_{\mathrm{in}} \cdot (\mathrm{ER} - 1)\mathrm{Dolp} \cdot \cos 4\varphi]^{2}}. \tag{14}$$

Similarly,

$$\mathrm{NeDolp}_{i,j} = \frac{1}{2x_{i,j}} * \left\{\frac{8[S0_{\mathrm{in}} \cdot (\mathrm{ER} + 1) + 2\bar{\chi}]^{2} - 3[S0_{\mathrm{in}} \cdot (\mathrm{ER} - 1)\mathrm{Dolp}]^{2}}{[S0_{\mathrm{in}} \cdot (\mathrm{ER} + 1) + 2\bar{\chi}]^{3}}\right\}. \tag{15}$$

Equations (14) and (15) show that the imaging accuracy of the system is related to the ER and the crosstalk ratio of the polarizer. Thus, we simulated 2 × 2 sets of polarizer pixels with orientations set at 0°, 45°, 90°, and 135° at the same time as shown in Fig. 7. The first model consisted of polarizer pixels with a 5 μm side and a 1 μm wide opaque region, while the second model consisted of polarizer pixels with a 12 μm pitch and a 2 μm wide opaque region. The boundary conditions at the x and y directions were made periodic such that the effective modeled structure was a repeating pattern of the 2 × 2 set, which is a good representation of patterns of actual devices. The 0° polarized source was then used at a distance of 3 μm above the aluminum wire layer in a downward direction. Accordingly, the ER could be calculated based on the transmittance of the pixel, which was

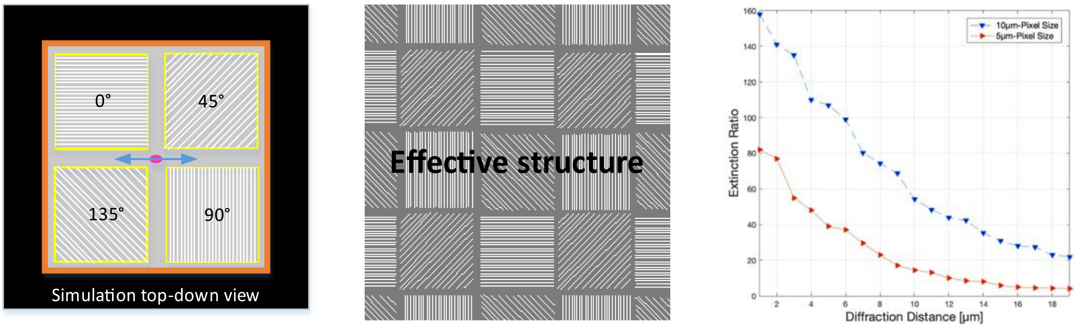

(a) (b) (c)

Fig. 7. (a) Top-down view of the simulated microgrid polarizer array. (b) Periodic boundary conditions around the set of four pixels created an effective structure that is representative of a real micropolarizer array and comprises a repeating pattern of "superpixels." (c) The ER curve as a function of the transmittance of the polarizer pixels with orientations set at 0° and 90°.

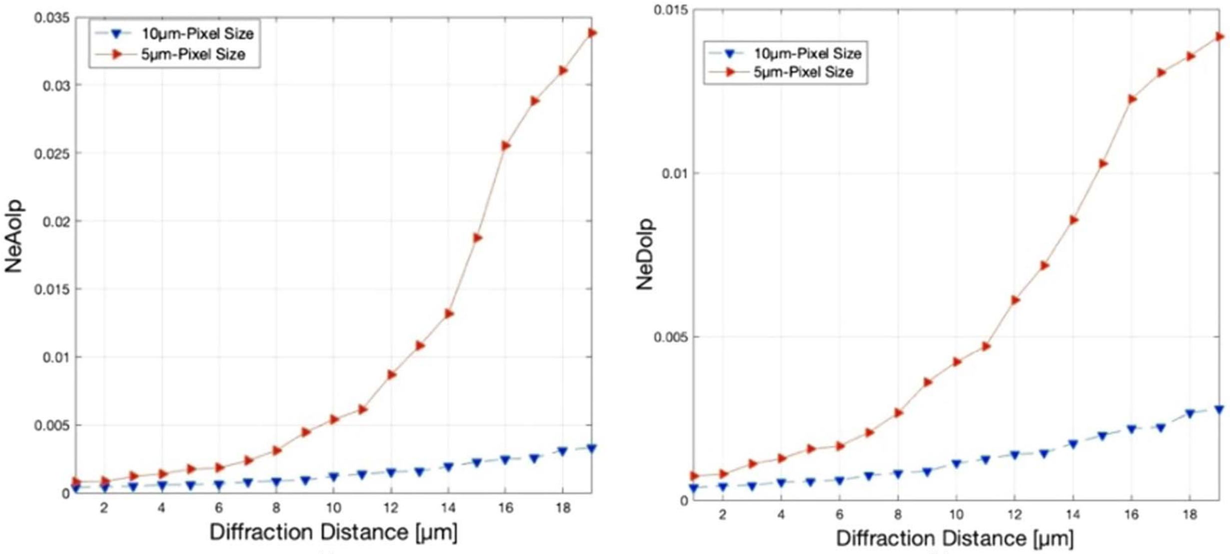

(a) (b)

Fig. 8. (a) Relationships between NeAolp and diffraction distance. (b) Relationships between NeDolp and diffraction distance.

measured by four 2D electric field monitors that were placed at a distance of 1 μm below the aluminum wire layer. The size of the monitor is the same as that of its corresponding polarizer.

By substituting the simulation results into Eqs. (14) and (15), the curves of NeAolp, NeDolp, and the diffraction distance can be obtained as shown in Fig. 8.

As the diffraction distance increases, the ER of the polarizer and the imaging accuracy decrease. For the same diffraction conditions, the red line exhibited better imaging accuracy. The simulation results also show that the polarization accuracy of the large-sized polarizer at 10 μm is equivalent to that of the small-sized polarizer at 2 μm. Therefore, the accuracy of Re-MPIS can be improved by improving diffraction distance or expanding the size of the polarizer unit.

The accuracy of the system is reflected in the sensitivity to errors given the solution process; the sensitivity of the system to errors can be expressed by the condition number (CN). The closer the CN is to unity, the higher the stability of the system. According to Eq. (16), the CNs of the two systems at different diffraction distances can be fitted as shown in Fig. 9:

$$\mathrm{CN} = \mathrm{cond}(M_c M_f) = \left\| M_c M_f \right\| \cdot \left\| (M_c M_f)^{-1} \right\| . \quad \textbf{(16)}$$

It can be observed from Fig. 9 that the CN of the transfer matrix of the 10 μm pixel size polarizer is always less than 2. This reflects the data fluctuation of the large-sized polarizer and indicates that it is more stable. This result is consistent with the conclusion above.

3. EXPERIMENTS AND RESULTS

As shown in Eqs. (14) and (15), we have established a multi-physical coupling mathematical model for polarimetric imaging systems. Substitution of the simulation results into the mathematical model indicates that the Re-MPIS has a higher accuracy and stability than MPIS. In the subsequent subsection, we build two experimental systems to test the ER, NeAolp, and NeDolp.

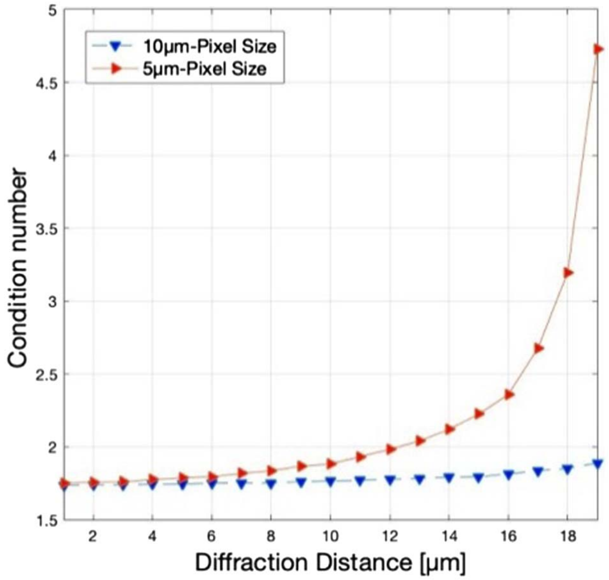

Fig. 9. CN of two polarizers at 10 μm.

A. Experimental MPIS System

The light source of the mounted polarimetric imaging is provided by an integrating sphere (Jingyi Photoelectric Corporation, CHN) with a light output aperture of 50 mm and a uniformity > 99%, followed by a collimator with a diameter of 15 mm and a focal length of 500 mm. The repositioning precision of the precision rotary table was 5 points. The filter transmission wavelength was in the range of 450–460 nm, and the cutoff band was equal to 1200 nm. The linear polarizer (LPVIS0200, Thorlab) had a transmittance > 0.8, and the ER was better than 1000. Thus, we can get uniform parallel light with precise and controllable polarization state. The light source was used to simulate a target source in remote sensing imaging applications. The test subject was the pixel-level polarcam polarimeter camera (4D Technology Corporation, USA) with pixel size of 7.4 μm × 7.4 μm. The entire system was placed on a platform as shown in Fig. 10.

The ER of the camera can be obtained experimentally. By rotating the linear polarizer, the maximum and minimum intensities will appear in the sensor, and the ER can be calculated based on the division of the light intensity. The average ER was calculated based on experimental data. To improve the measurement accuracy, we rotated the linear polarizer at 2° intervals and acquired 100 images at each interval. The light intensity response of each subpixel was fitted based on the data fitting method. The maximum light intensity after fitting was recorded as ε, and the minimum light intensity value was recorded as η. Once the light intensity in a superpixel was obtained, we obtained a set of solutions for DOLP and AOLP. We used the photoelectronic numbers received by superpixels (PNRS) to assess whether the magnitude of the error was equal. The value of PNRS was equal to the total photoelectronic numbers of four pixels in a superpixel. We used the average PNRS to represent the random error of the system.

B. Experimental Re-MPIS

The imaging accuracy of the Re-MPIS is affected by many factors, such as the registration of the primary image plane with the target surface, the distortion of the relay lens, and others. To verify the simulation results conveniently and eliminate the interference of other factors, we used microscopes instead of a relay system to test the polarizer device at the first stage of the Re-MPIS research endeavor.

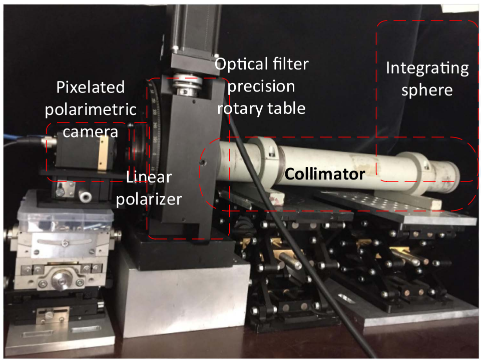

Fig. 10. Experimental MPIS.

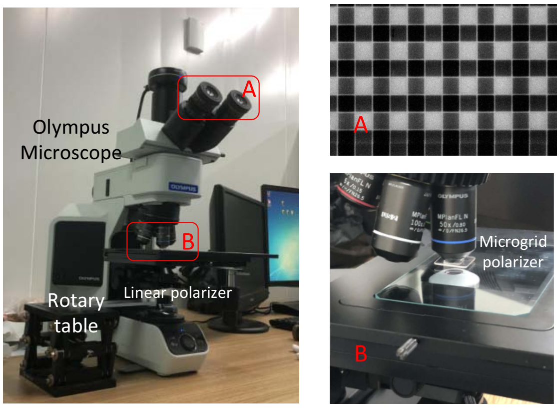

Fig. 11. Experimental Re-MPIS.

The system used an Olympus microscope (Olympus BX53M) [23], which provided a high-intensity, white-light-emitting diode (LED) light source with a wavelength in the range of 450–460 nm. Polarization filters were placed on the light source path. Controllable polarization light was obtained by controlling the rotating filter of the platform. The minimum focusing scale of the microscope was 1 μm, and the optical system was calibrated at infinity. The experimental image was collected with stream image analysis software. The fabricated microgrid polarizer measured ERs $> 80:1$ with the pixel size of 13 μm × 13 μm. The test system is shown in Fig. 11.

We carefully rotated the wheel with fine adjustments until a clear image appeared on the screen. To ensure that the noise response in the two system was the same, we needed to readjust the exposure time ceaselessly to make the values of the PNRS of the two systems as close as possible. The other procedures were the same as those listed above. We rotated the linear polarizer and collected 100 pictures at each angular interval. According to the intensity response of each pixel, we recorded the average ER and PNRS values.

C. Experimental Results and Discussion

Given the nonuniformity of the camera image surface, we used the average ER of the target to represent the ER of a polarization camera. To simplify the calculation, the experiment was carried out in a 60 pixel × 60 pixel area in the middle of the target surface. The ER distribution is shown in Fig. 12.

A set of comparison pictures is shown in Fig. 13. According to the gray values of the collected images, we can calculate the polarization state of the incident light based on Eqs. (4) and (5). Given that it is difficult to measure the crosstalk ratio of each pixel, we used the simulation method to assign these values. According to Eqs. (17) and (18), we can estimate the imaging accuracy of the two polarization imaging systems:

$$\mathrm{NeDolp} = \sqrt{\left\{ \sum_{n=1}^{100} [(\sum_{i,j}^{i=30,j=30} \mathrm{Dolp}_{i,j}) / 900 - \overline{\mathrm{Dolp}_n}]^2 \right\} / 100}, \tag{17}$$

$$\mathrm{NeAolp} = \sqrt{\left\{ \sum_{n=1}^{100} [(\sum_{i,j}^{i=30,j=30} \mathrm{Aolp}_{i,j}) / 900 - \overline{\mathrm{Aolp}_n}]^2 \right\} / 100}. \tag{18}$$

According to the calculated ER values listed in Table 1, the microgrid polarimetric relay imaging system is better than the traditionally mounted polarimetric system. The extinction

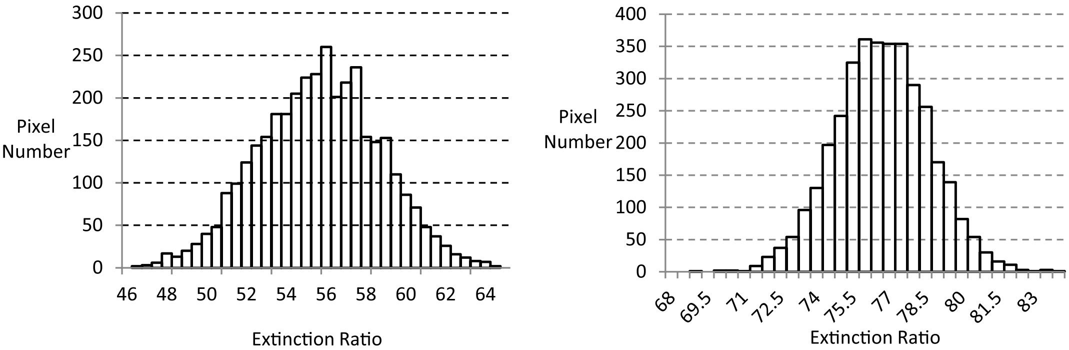

Fig. 12. ER distributions.

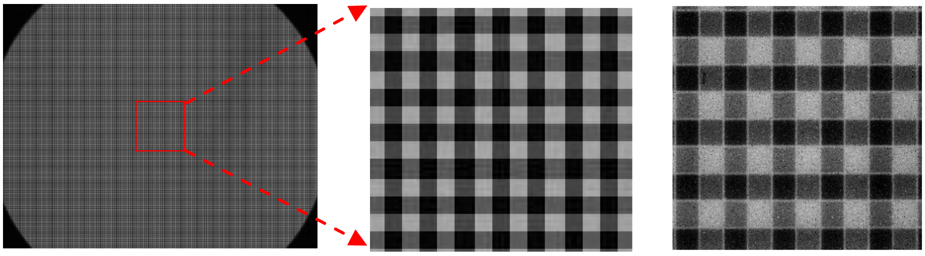
(a) (b) (c)

Fig. 13. (a) Acquired images using the MPIS. (b) Partial enlargement of images using the MPIS. (c) Partial enlargement of images using the Re-MPIS.

Table 1. Experimental Results

Style	Extinction Ratio	NeDolp	NeAolp	PNRS
Mount	54.2	13.98%	7.40°	10.7ke-
Relay	76.4	9.62%	5.15°	11.1ke-

ratio of the relay system is 40.2% higher than that of the mount system, the NeDolp of the relay system is 31.2% higher than that of the mount system, and the NeAolp of the relay system is 30.4% higher than that of the mount system. Even though the experimental results are quite different from those evoked by simulations, they are still credible. The main reason for the gap relates to the facts that (1) the ultraprecision machining technology is not mature, and the uniformity and accuracy of the microgrid polarizer is poor [as observed in Fig. 13(c), there are impurities in the acquired images], and (2) in addition to the optical crosstalk, there is still electronic crosstalk among sensor pixels (this has not been discussed in this study). The theoretical simulation and experimental results are basically the same within the permitted error bounds. Although the current experimental conditions are not ideal, the feasibility of the new system has been proved through simulation and experiments. In the next step, we will focus on the improvement of the relay experiment system, including the measurement of the crosstalk ratio in the experiment and the registration of the microgrid polarizer with the sensor.

4. CONCLUSION

Given the poor ER and accuracy responses of existing polarimetric imaging systems owing to the use of nanowire filters, we have proposed a microgrid polarimeter relay imaging system that effectively suppresses optical crosstalk and increases imaging accuracy. Compared with the traditional polarimetric imaging system, Re-MPIS has higher degrees of freedom, and thus it could realize multimodal imaging by switching different filters in and out of the optical path. Specifically, for airborne imaging systems, MPIS are undesirable for use in sensitive applications, in which high transmittances are necessary, because the microgrid polarizer reduces the amount of light that reaches the sensor pixels. The polarizer concurrently provides the Re-MPIS with the capacity to operate in high-transmittance or filter modes as needed. Based on the FDTD simulation result, we define a new parameter that could directly reflect the degree of crosstalk. Compared with the previous way to express crosstalk, the new parameter will not be affected by the intensity of target light, and it could be used to establish a polarization vector transfer model. Since the existing imaging accuracy model of polarimetric systems only considers the influence of ER, SNR, and sensor error on the imaging quality, and ignores the error caused by optical crosstalk, we have thus deduced a more specific mathematic model of multi-coupling physical parameters. Compared with the existing model, the new physical model is well suited to more realistic scenarios, such as the case in which the crosstalk error is larger than the random error in instances at which the target spectral information differs considerably from the light source used for the nonuniformity correction. In that case, the traditional model will become unreliable.

The experimental outcomes exhibited minor differences compared to the simulation outcomes. This was mainly attributed to the fact that the experimental system was not complete. Numerous shortcomings exist in the Re-MPIS platform. Thus, solutions to improve the experimental conditions will be the subject of future investigations.

Funding. National Natural Science Foundation of China (61675202, 61627819, 61727818); National Youth Foundation of China (61905240).

Disclosures. The authors declare no conflicts of interest.

REFERENCES

1. Z.-Y. Chen, L.-S. Yan, Y. Pan, L. Jiang, A.-L. Yi, W. Pan, and B. Luo, “Use of polarization freedom beyond polarization-division multiplexing to support high-speed and spectral-efficient data transmission,” Light Sci. Appl. **6**, e16207 (2017).
2. Y. Liu, T. York, W. Akers, G. Sudlow, V. Gruev, and S. Achilefu, “Complementary fluorescence-polarization microscopy using division-of-focal-plane polarization imaging sensor,” Biomed. Opt. **17**, 116001 (2012).
3. M. Wang, R. Salut, H. Lu, M.-A. Suarez, N. Martin, and T. Grosjean, “Subwavelength polarization optics via individual and coupled helical traveling-wave nanoantennas,” Light Sci. Appl. **8**, 76 (2019).
4. M. Zhang, X. Wu, N. Cui, N. Engheta, and J. Van der Spiegel, “Bioinspired focal-plane polarization image sensor design: from application to implementation,” Proc. IEEE **102**, 1435–1449 (2014).
5. E. S. Sedov, Y. G. Rubo, and A. V. Kavokin, “Polariton polarization rectifier,” Light Sci. Appl. **8**, 79 (2019).
6. A. Basiri, X. Chen, J. Bai, P. Amrollahi, J. Carpenter, Z. Holman, and C. Want, and Y. Yao, “Nature-inspired chiral metasurfaces for circular polarization detection and full-Stokes polarimetric measurements,” Light Sci. Appl. **8**, 78 (2019).
7. S. Bear Powell and V. Gruev, “Calibration methods for division-of-focal-plane polarimeters,” Opt. Express **21**, 21039–21055 (2013).
8. L. Li, T. Li, X.-M. Tang, S.-M. Wang, Q.-J. Wan, and S.-N. Zhu, “Plasmonic polarization generator in well-routed beaming,” Light Sci. Appl. **4**, e330 (2015).
9. Y. Maruyama, T. Terada, T. Yamazaki, Y. Uesaka, M. Nakamura, Y. Matoba, K. Komori, Y. Ohba, S. Arakawa, and Y. Hirasawa, “3.2-MP back-illuminated polarization image sensor with four-directional air-gap wire grid and 2.5-μm pixels,” IEEE Trans. Electron. Devices **65**, 2544–2551 (2018).
10. H. Park and K. B. Crozier, “Elliptical silicon nanowire photodetectors for polarization-resolved imaging,” Opt. Express **23**, 7209–7216 (2015).
11. Z. Chen, X. Wang, S. Pacheco, and R. Liang, “Impact of CCD camera SNR on polarimetric accuracy,” Appl. Opt. **53**, 7649–7656 (2014).
12. Y. Li, W. J. Zhang, and J. Y. Chen, “Modeling and simulation of target detection in polarized scene,” Opt. Precis. Eng. **25**, 2233–2243 (2017).
13. “4D’s polarimetric imaging camera based on nano-wire filter [EB/OL],” https://www.4dtechnology.com/products/polarimeters/polarcam/.
14. A. A. Cruz-Cabrera, S. A. Kemme, J. R. Wendt, R. R. Boye, T. R. Carter, and S. Samora, “Polarimetric imaging cross talk effects from glue separation between FPA and micropolarizer arrays at the MWIR,” Proc. SPIE **6478**, 64780Q (2007).
15. S. A. Kemme, A. A. Cruz-Cabrera, P. Nandy, R. R. Boye, J. R. Wendt, T. O. Carter, and S. Samora, “Micropolarizer arrays in the MWIR for snapshot polarimetric imaging,” Proc. SPIE **6556**, 655604 (2007).
16. D. Vorobiev, Z. Ninkov, and M. Gartley, “Polarization in a snap: imaging polarimetry with micropolarizer arrays,” Proc. SPIE **9099**, 909904 (2017).

17. H. Sun, D. J. Wang, C. Chen, K. Long, and X. Sun, “Effect of. sensor SNR and extinction ratio on polarimetric imaging error for nanowire-based systems,” Appl. Opt. **57**, 7344–7351 (2018).
18. R. Perkins and V. Gruev, “Signal-to-noise analysis of Stokes parameters in division of focal plane polarimeters,” Opt. Express **18**, 25815–25824 (2010).
19. M. W. Jones and C. M. Persons, “Performance predictions for micro-polarizer array imaging polarimeters,” Proc. SPIE **6682**, 668208 (2007).
20. T. C. Choy, *Effective Medium Theory: Principles and Applications* (Oxford University, 1999), Vol. **165**.
21. H. Du, H. Chen, H. Gong, T. G. Wang, C. Sun, S. W. Lee, and L. S. Wen, “Use of effective medium theory to model the effect of the microstructure on dc conductivity of nano-titanium films,” Appl. Surf. Sci. **233**, 99–104 (2004).
22. S. Roussel, M. Boffety, and F. Goudail, “Polarimetric precision of micropolarizer grid-based camera in the presence of additive and Poisson shot noise,” Opt. Express **26**, 29968–29982 (2018).
23. Olympus BX53M metallographic microscope. http://www.bio-equip.com/show1equip.asp?equipid=4026539